Nature of polarization in wide-bandgap semiconductor detectors under high-flux irradiation: Application to semi-insulating $Cd_{1-x}Zn_xTe$

Derek S. Bale* and Csaba Szeles
eV PRODUCTS, Compound Semiconductor Group II-VI Inc., Saxonburg, Pennsylvania 16056, USA
(Received 7 September 2007; published 14 January 2008)

In this paper, we theoretically investigate the mechanism of polarization in wide-bandgap semiconductor radiation detectors under high-flux x-ray irradiation. Our general mathematical model of the defect structure within the bandgap is a system of balance laws based on carrier transport and defect transition rates, coupled together with the Poisson equation for the electric potential. The dynamical system is self-consistently evolved in time using a high-resolution wave propagation numerical algorithm. Through simulation, we identify and present a sequence of dynamics that determines a critical flux of photons above which polarization effects dominate. Using the experience gained through numerical simulation of the full set of equations, we derive a reduced system of conservation laws that describe the dominant dynamics. A multiple scale perturbation analysis of the reduced system is shown to yield an analytical dependence of the maximum sustainable flux on key material, detector, and operating parameters. The predicted dependencies are validated for 16×16 pixel CdZnTe monolithic detector arrays subjected to a high-flux 120 kVp x-ray source.

DOI: 10.1103/PhysRevB.77.035205 PACS number(s): 07.85.Fv, 71.55.Gs

I. INTRODUCTION

There is growing interest in the potentials of pulse mode CdZnTe detector technology for high-flux high-speed energy selective or hyperspectral x-ray imaging. The energy sensitivity provided by CdZnTe opens up a range of intriguing new potential applications for this detector technology in medical, industrial, and security imaging and tomography. However, imaging applications typically require photon flux fields that generate very high count rates within the semi-insulating CdZnTe crystal. In particular, medical computer tomography applications represent a large potential market for this technology but require detectors capable of handling count rates of $(20-200)\times10^6$ counts/mm^2 s[1].

One of the greatest challenges in applying pulse mode CdZnTe detector technology to applications requiring such high count rates is avoiding buildup of charge within the crystal, which collapses the electric field and results in catastrophic device failure (i.e., *polarization*).[1,2] Therefore, one must design these devices such that the charge generated by the x-ray radiation is removed from the device at a sufficiently high rate through both drift and recombination. The choice of material, detector, and operating parameters is paramount to achieving high charge throughput for devices based on CdZnTe or any semiconducting detector material. Clearly, a careful choice of both material and detector design parameters, as well as operating conditions, must be predicated on a fundamental understanding of the dependence of the onset of polarization on such critical parameters and conditions.

In Ref. 3, Du *et al.* modeled the temporal response of CdZnTe under intense irradiation by considering a bandgap with a single acceptor and donor level. They applied a finite element numerical algorithm to the resulting equations and demonstrated distortions in the electric field and carrier concentrations under high-flux irradiation. In this paper, we develop a general mathematical model of the bandgap that includes an arbitrary number of donor and acceptor defects. Our model is a system of nonlinear balance laws based on carrier transport and defect transition rates, coupled together with the Poisson equation for the electric potential. The resulting dynamical system is numerically evolved in time using flux-conservative wave propagation algorithms developed for conservation laws with spatially varying flux functions.[4–6] Our high-resolution numerical algorithm preserves carrier number densities while suppressing numerical instabilities often caused by large gradients that develop in the solutions under the extreme conditions encountered in simulations of high-flux x-ray applications. In Sec. II, we present the details of both our mathematical model of the bandgap and its numerical solution.

Through simulation, we have identified a sequence of dynamics that determines a critical flux of photons above which polarization effects dominate, resulting in catastrophic device failure. In Sec. III, we illustrate this sequence of events through a specific set of example simulations. Using experience gained through a large matrix of such simulations, we have derived a reduced system of conservation laws that describe the dominant dynamics relevant for a polarizing detector. In Sec. IV, we use a multiple scale perturbation analysis, for which details can be found in Ref. 7, on the reduced system of equations to derive an analytic expression describing the dependence of the maximum sustainable flux on key material, operating, and detector design parameters. The predicted dependencies on bias voltage and temperature are experimentally validated for 16×16 pixel CdZnTe monolithic detector arrays in Secs. IV C 1 and IV C 2, respectively.

II. MODEL OF THE BANDGAP DEFECT STRUCTURE

In this work, we consider a semi-insulating, wide-bandgap semiconductor with M_A distinct acceptor defect levels within the bandgap and M_D donor levels. The presence of the energy levels is assumed due to electronic point defects within the crystal. Many such defect levels have been mea-

 ©2008 The American Physical Society

sured within CdTe and CdZnTe.[8] Therefore, the number of energy levels associated with acceptor defect levels, M_A, as well as the number of donor levels, M_D, are assumed arbitrary. Each acceptor has total concentration $\mathcal{P}^l$ and an energy E_A^l within the bandgap, where $l \in \{1,2,\ldots,M_A\}$ is used to enumerate individual levels. Similarly, donor levels have concentrations denoted by $\mathcal{N}^k$ and energy levels by E_D^k, with $k \in \{1,2,\ldots,M_D\}$. The top edge of the valence band is defined to be the zero of energy so that the bottom edge of the conduction band is simply the bandgap energy, $E_c = E_g$ (e.g., $E_g \sim 1.54$ eV at room temperature in CdZnTe). Further, we assume that the semiconductor is nondegenerate so that the Fermi energy E_F is far from the band edges relative to the thermal energy $k\mathcal{T}$.

A. Carrier transition rates

The concentration of free holes in the valence band is denoted by P, while the concentration of trapped holes in the lth acceptor defect is denoted by $\hat{P}^l$. The free electron concentration is denoted by N and that of trapped electrons in the kth donor level is denoted by $\hat{N}^k$. Equilibrium concentrations for the free carriers, denoted by P_0 and N_0, as well as the equilibrium concentrations of trapped carriers, $\hat{P}_0^l$ and $\hat{N}_0^k$, are governed, as usual, by the position of the Fermi energy under the charge neutrality condition.[8] In what follows, we use these equilibrium values to scale the dynamical system for the purpose of numerical, as well as analytical, solution.

The attractive potential of ionized traps (i.e., unoccupied donors and occupied acceptors) gives rise to trapping of free electrons onto donor sites and free holes to acceptor sites. We also consider detrapping in which a trapped carrier is thermally excited back to the energy band. The rates at which electrons are trapped and detrapped are given by

$$\Lambda_{\downarrow:D}^k = \sigma_D^k \theta \mathcal{N}^k \left(1 - \frac{\hat{N}^k}{\mathcal{N}^k}\right), \tag{1a}$$

$$\Lambda_{\uparrow:D}^k = \nu_D^k \exp\left(-\frac{E_g - E_D^k}{k\mathcal{T}}\right), \tag{1b}$$

respectively, where σ_D^k is the capture cross section of the kth defect level, θ is the thermal velocity of the carriers, and ν_D^k is an escape frequency independent of both free and trapped carrier concentrations. It is typical to choose the escape frequency ν_D^k so that the detailed balance of thermal equilibrium is satisfied. In general, however, we leave the escape frequencies as free parameters due to the fact that the assumption of the principle of detailed balance may not be valid for carrier dynamics driven far from equilibrium. The rates at which holes are trapped and detrapped from the lth acceptor are denoted by $\Lambda_{\downarrow:A}^l$, and $\Lambda_{\uparrow:A}^l$, respectively. Their functional forms are similar to Eqs. (1a) and (1b), with the electron parameters and concentrations replaced by analogous hole quantities.

Detrapping at a rate given by Eq. (1b) is not the only transition we consider for a trapped carrier. For example, a trapped electron may undergo recombination with a free hole in the valence band. The recombination rate is taken to depend on the concentration of trapped electrons, while its inverse transition, consisting of an electron excited from the valence band to the kth donor level, is taken to be driven by temperature. The rate of electron recombination and its inverse process are given by

$$\Upsilon_{\downarrow:D}^k = \chi_D^k \theta \hat{N}^k, \tag{2a}$$

$$\Upsilon_{\uparrow:D}^k = \mu_D^k \exp\left(-\frac{E_D^k}{k\mathcal{T}}\right), \tag{2b}$$

where χ_D^k is the recombination cross section, and μ_D^k, like ν_D^k, is an escape frequency and is assumed to have no dependence on the concentrations of free or trapped carriers. Because an occupied donor is neutral, there is no strong Coulomb potential driving recombination as there is for electron trapping. Consequently, the recombination cross section, χ_D^k is assumed to be small compared to the trapping cross section, $\chi_D^k \ll \sigma_D^k$. The recombination transition for trapped holes is denoted by $\Upsilon_{\downarrow:A}^l$, and the rate of its inverse transition is given by $\Upsilon_{\uparrow:A}^l$. Like the hole rates for trapping and detrapping, these rates have functional forms similar to the electron rates in Eqs. (2a) and (2b), with the electron parameters and concentrations replaced by analogous hole quantities. It is also true that the recombination of trapped holes is a weaker process than hole trapping, so we take $\chi_A^l \ll \sigma_A^l$. We also point out that, like μ_D^k, μ_A^l is the escape frequency from the lth acceptor level and can be chosen using detailed balance in thermal equilibrium or a steady state of the dynamical system.

Finally, semi-insulating CdZnTe near equilibrium typically has free carrier concentrations $<10^6/\mathrm{cm}^3$,[9] so direct band-to-band recombination rates are quite low. In steady states generated by high-flux x-ray sources, however, the concentrations of free carriers can be many orders of magnitude larger. In this case, the probability that a free hole will directly recombine with a free electron is dramatically increased. Direct band-to-band transitions, therefore, are taken as a sink for both free electrons and holes in the form

$$S_{bb} = \sigma_{bb} \theta (NP - N_0 P_0), \tag{3}$$

where σ_{bb} is the cross section for this transition, and N_0 and P_0 are the free electron and hole concentrations in equilibrium, respectively.

B. Dynamical equations

Now that we have introduced the transitions that we consider in our model, we can write down the system of partial differential equations that govern the dynamical response of a parallel plate detector placed under bias and subjected to an x-ray flux. The bias voltage is considered to be high enough that diffusion currents can be neglected relative to drift currents. Under these conditions, the set of dependent variables $\{N, P, \hat{N}^k, \hat{P}^l, \Phi\}$ depends on one space dimension Z and time T. The balance laws that include carrier transport, trapping, detrapping, and recombination are

$$\frac{\partial}{\partial T}N + \frac{\partial}{\partial Z}[\mu_e EN] = \sum_{k=1}^{M_D}[\Lambda^k_{\uparrow:D}\hat{N}^k - \Lambda^k_{\downarrow:D}N] + \sum_{l=1}^{M_A}[\Upsilon^l_{\uparrow:A}(\mathcal{P}^l - \hat{P}^l) - \Upsilon^l_{\downarrow:A}N] - S_{bb} + \Psi, \quad (4a)$$

$$\frac{\partial}{\partial T}P - \frac{\partial}{\partial Z}[\mu_h EP] = \sum_{k=1}^{M_D}[\Upsilon^k_{\uparrow:D}(\mathcal{N}^k - \hat{N}^k) - \Upsilon^k_{\downarrow:D}P] + \sum_{l=1}^{M_A}[\Lambda^l_{\uparrow:A}\hat{P}^l - \Lambda^l_{\downarrow:A}P] - S_{bb} + \Psi, \quad (4b)$$

$$\frac{\partial}{\partial T}\hat{N}^k = \Lambda^k_{\downarrow:D}N - \Lambda^k_{\uparrow:D}\hat{N}^k + \Upsilon^k_{\uparrow:D}(\mathcal{N}^k - \hat{N}^k) - \Upsilon^k_{\downarrow:D}P, \quad (4c)$$

$$\frac{\partial}{\partial T}\hat{P}^l = \Lambda^l_{\downarrow:A}P - \Lambda^l_{\uparrow:A}\hat{P}^l + \Upsilon^l_{\uparrow:A}(\mathcal{P}^l - \hat{P}^l) - \Upsilon^l_{\downarrow:A}N, \quad (4d)$$

where we have introduced the free carrier generation source $\Psi(Z,T)$ and the electric field $E(Z,T)=-\partial\Phi/\partial Z$. We point out that the free carrier concentrations, namely, N and P, are affected by transitions into and out of all donor and acceptor defect levels through trapping and recombination processes previously discussed. This influence is captured by the summation over all defect levels on the right hand side of Eqs. (4a) and (4b). The concentrations of trapped carriers $\hat{N}^k$ and $\hat{P}^l$, on the other hand, are only affected by transitions to and from the energy bands, as indicated by the source terms of Eqs. (4c) and (4d).

Since the free carrier flux depends on the electric field, Eqs. (4a)–(4d) must be coupled to the Poisson equation for the electric potential,

$$\frac{\partial}{\partial Z}\left[\epsilon_0\frac{\partial}{\partial Z}\Phi\right] = q\left\{P - \sum_{l=1}^{M_A}(\mathcal{P}^l - \hat{P}^l) - N + \sum_{k=1}^{M_D}(\mathcal{N}^k - \hat{N}^k)\right\}. \quad (4e)$$

Note that this system of partial differential equations is nonlinear in both the source term and the transport fluxes.

C. Numerical solution

There are two major challenges in developing numerical solutions to Eqs. (4a)–(4e) when Ψ is an intense source of free carriers due to x rays. The first challenge stems from the fact that the evolution of this system has vastly different time scales associated with both the charge transport, and the charge generation, trapping, and recombination processes. For example, measurements of the electron mobility in CdZnTe typically yield values around 1000 $cm^2\,V^{-1}\,s^{-1}$.[8,10] Applied fields of several thousand V/cm are common and produce transport time scales in the hundred nanosecond range ($\sim 10^{-7}$ s) for 5–10 mm thick detectors. On the other hand, applying the transition rates in Eqs. (1a) and (1b) with energy levels and other defect parameters consistent with the composition-dependent charge transport properties of CdZnTe (Refs. 8 and 9) results in shallow donors and acceptors that can trap and detrap on a tens of picosecond scale ($\sim 10^{-11}$ s) and deep defect levels that can detrap on a time scale of seconds ($\sim 10^0$ s). Therefore, Eqs. (4a)–(4e) contain potentially 12 orders of magnitude separating the dynamical time scales for these processes, making the system very stiff numerically.

A second challenge originates from the fact that equilibrium concentrations of free carriers in CdZnTe are typically (10^4-10^6) cm^3.[9] Therefore, assuming a pair creation energy of $\sim$4.5–5 eV,[11] a single 100 keV photon can more than double the concentration of free carriers within a small region of the interaction. Further, in Sec. III, we show that high-flux x-ray sources considered here produce interactions close enough in time to increase the local concentration of free carriers not by a factor of 2 but by orders of magnitude. As a consequence, carrier concentrations can have large spatial gradients associated with their transport that are well known to cause numerical instabilities.[5,6] In the remainder of this section, therefore, we discuss our choice of scaling and numerical implementation that enables the accurate and stable integration of Eqs. (4a)–(4e) under conditions of intense x-ray irradiation.

1. Scaling the equations

Appropriate scaling of independent, as well as dependent variables, is an important part of the numerical solution of any system, but due to the very large range of relevant time scales, it is crucial in solving Eqs. (4a)–(4e). To that end, we define nondimensional free carrier densities p and n by scaling the physical concentrations P and N by their equilibrium values P_0 and N_0, so that

$$P = P_0 p, \quad N = N_0 n. \quad (5a)$$

Nondimensional trapped carrier concentrations $\hat{p}^l$ and $\hat{n}^k$ are defined by scaling their dimensional counterparts $\hat{P}^l$ and $\hat{N}^k$ by the relevant total defect concentration,

$$\hat{P}^l = \mathcal{P}^l\hat{p}^l, \quad \hat{N}^k = \mathcal{N}^k\hat{n}^k. \quad (5b)$$

In addition to scaling the dependent field variables, we must choose an appropriate space and time scale that defines nondimensional independent variables for space z and time t as

$$Z = Lz, \quad T = \tau t. \quad (6)$$

In the numerical solutions presented in this paper, we take L to be the detector thickness and the electron transit time as our time scale so that $\tau=\tau_{tr}=L^2/(\mu_e\mathcal{V})$.

Substituting these nondimensional variables into Eqs. (4a)–(4e) and defining a vector of dependent state variables $\boldsymbol{q}(z,t)=[n,p,\hat{n}^k,\hat{p}^l]^T$, we can rewrite Eqs. (4a)–(4d) in vector form so that the dynamical system (4a)–(4e) can be written as

$$\partial_t\boldsymbol{q}(z,t) + \partial_z\boldsymbol{f}(\boldsymbol{q},z) = \boldsymbol{s}_{\Updownarrow}(\boldsymbol{q},t), \quad (7a)$$

$$\partial_z^2 \phi = \gamma \left[\alpha \left(p - \sum_{l=1}^{M_A} \eta_A^l (1 - \hat{p}^l) \right) - \left(n - \sum_{k=1}^{M_D} \eta_D^k (1 - \hat{n}^k) \right) \right]. \tag{7b}$$

In the above equations, we have introduced the flux vector $\boldsymbol{f}(\boldsymbol{q},z)$ and the source vector $\boldsymbol{s}_{\Updownarrow}(\boldsymbol{q},t)$ and defined the nondimensional parameters

$$\alpha = \frac{P_0}{N_0}, \quad \eta_D^k = \frac{\mathcal{N}^k}{N_0}, \quad \eta_A^l = \frac{\mathcal{P}^l}{P_0}, \quad \gamma = \frac{qL^2 N_0}{\epsilon_0 \mathcal{V}}. \tag{8}$$

Note that the dynamical equations for the physical free carrier concentrations N and P, namely Eqs. (4a) and (4b), are the only equations that contain a transport flux (i.e., spatial derivative $\partial/\partial Z$). Therefore, the flux defined in Eq. (7a) has the nondimensional vector form

$$\boldsymbol{f}(\boldsymbol{q},z) = [e(z)n, -\mu e(z)p, 0, \ldots, 0]^T, \tag{9}$$

where $e(z) = \frac{L}{\mathcal{V}} E(Z)$ is the nondimensional electric field, and $\mu = \mu_h/\mu_e$. Finally, in Eq. (7a), we have introduced the bandgap transition source, $\boldsymbol{s}_{\Updownarrow}(\boldsymbol{q},t)$, which represents a scaled version of the right hand side of Eqs. (4a)–(4d) and has the form

$$\boldsymbol{s}_{\Updownarrow} = \tau \begin{pmatrix} \sum_{k=1}^{M_D} (\eta_D^k \Lambda_{\uparrow:D}^k \hat{n}^k - \Lambda_{\downarrow:D}^k n) + \sum_{l=1}^{M_A} (\alpha \eta_A^l \Upsilon_{\uparrow:A}^l (1 - \hat{p}^l) - \Upsilon_{\downarrow:A}^l n) - S_{bb} + \Psi \\ \sum_{k=1}^{M_D} \left(\frac{\eta_D^k}{\alpha} \Upsilon_{\uparrow:D}^k (1 - \hat{n}^k) - \Upsilon_{\downarrow:D}^k p \right) + \sum_{l=1}^{M_A} (\eta_A^l \Lambda_{\uparrow:A}^l \hat{p}^l - \Lambda_{\downarrow:A}^l p) - S_{bb} + \Psi \\ \left(\frac{1}{\eta_D^k} \right) \Lambda_{\downarrow:D}^k n - \tilde{\Lambda}_{\uparrow:D}^k \hat{n}^k + \Upsilon_{\uparrow:D}^k (1 - \hat{n}^k) - \frac{\alpha}{\eta_D^k} \Upsilon_{\downarrow:D}^k p \\ \left(\frac{1}{\eta_A^l} \right) \Lambda_{\downarrow:A}^l p - \Lambda_{\uparrow:A}^l \hat{p}^l + \Upsilon_{\uparrow:A}^l (1 - \hat{p}^l) - \left(\frac{1}{\alpha \eta_A^l} \right) \Upsilon_{\downarrow:A}^l n \end{pmatrix}. \tag{10}$$

System (7a) and (7b) is in a standard mathematical form for a balance law, and it is this scaled form that we numerically solve.

2. Numerical implementation

We implement a split-scheme approach so that we can apply the appropriate numerical algorithm to both challenges previously mentioned. The basic split-scheme solution process over a single time step Δt is as follows:

(1) transport [solve $\partial_t \boldsymbol{q} + \partial_z \boldsymbol{f}(\boldsymbol{q},z) = 0$ over a half time step $\Delta t/2$];

(2) source [solve $\partial_t \boldsymbol{q} = \boldsymbol{s}_{\Updownarrow}(\boldsymbol{q},t)$ over a full time step Δt];

(3) transport [solve $\partial_t \boldsymbol{q} + \partial_z \boldsymbol{f}(\boldsymbol{q},z) = 0$ over a another half time step $\Delta t/2$]; and

(4) field [solve Poisson Eq. (7b) with updated concentrations].

The first three steps of this process evolve Eq. (7a) forward in time by a single time step Δt. The transport steps neglect the source term and move carrier concentrations along characteristics, while the source step neglects the spatial derivatives and modifies the concentrations according to the source term $\boldsymbol{s}_{\Updownarrow}$ defined in Eq. (10). The fourth step of the solution process assures that the electric field is self-consistently evolved in time with the carrier concentrations.

Previously, we discussed the fact that in problems involving a high-flux x-ray source, carrier concentrations in Eqs. (7a) and (7b) will develop large gradients during transport. The application of a simple finite difference numerical scheme to such gradients often introduces spurious oscillations that can, in turn, trigger numerical instabilities. Therefore, during the transport steps of the solution process, we have implemented a high-resolution wave propagation algorithm developed for conservation laws with spatially varying flux functions.[4,5] This algorithm is based on the original wave propagation technique developed by LeVeque,[6,12] and designed to limit spurious numerical oscillations near large gradients while maintaining high accuracy elsewhere. The algorithm is flux conservative so that carrier number densities are conserved to machine precision during the transport steps of the evolution process. Conservation of carriers is a desired numerical property due to the fact that, neglecting the generation source and losses at boundaries, Eqs. (7a) and (7b) conserve the total number densities of both electrons and holes up to that lost due to recombination transitions. Finally, a standard Rosenbrock method designed for stiff systems is used during the source step of the solution process.

III. SIMULATION RESULTS

A large matrix of simulations has been completed in which we varied the number of donors M_D, the number of acceptors M_A, as well as the individual defect level parameters such as total concentrations $\mathcal{P}^l$ and $\mathcal{N}^k$, ionization energies E_A^l and E_D^k, and trapping cross sections σ_A^l and σ_D^k. In

TABLE I. Bandgap structure and defect level parameters.

Bandgap defect structure					
Acceptor levels					
l	E_A^l (eV)	$\mathcal{P}^l$ (cm^{-3})	σ_A^l (cm^2)	χ_A^l (cm^2)	g_A^l
1	0.15	1×10^{11}	2×10^{-13}	3×10^{-14}	4
2	0.60	1×10^{12}	2×10^{-13}	3×10^{-14}	4
Donor levels					
k	E_D^k (eV)	$\mathcal{N}^k$ (cm^{-3})	σ_D^k (cm^2)	χ_D^k (cm^2)	g_D^k
1	1.558	1.075×10^{12}	5×10^{-13}	3×10^{-14}	2
2	0.802	1×10^{11}	5×10^{-13}	3×10^{-14}	2

this matrix, we also varied the operating conditions and detector design parameters such as bias voltage $\mathcal{V}$, temperature $\mathcal{T}$, and detector thickness L. The source of photons was taken to be that of an x-ray tube with a differential energy spectrum modeled by[13]

$$\frac{1}{A\Delta t}\frac{dn_\gamma}{de} = \frac{qF_A I}{2\pi r^2}\left(\frac{T_e}{e} - 1\right)\exp\left(-\sum_i \mu_i(e)\delta_i\right), \qquad (11)$$

where I is the tube current, F_A is a constant representing the bremsstrahlung production per incident electron energy, $T_e = qV_t$ is the incident electron energy proportional to the tube voltage V_t, and e is the energy of the emanating photon. The exponential term describes the attenuation caused by the ith filter layer with thickness δ_i and attenuation coefficient $\mu_i(e)$. In all simulations presented here, the tube was turned on at time $t=0$, and the voltage and current were held constant until the transient dynamics relaxed to a steady state. The resulting steady state profiles of the electric field, carrier concentrations, carrier lifetimes, and charge induction maps suggest a clear sequence of dynamics that serves to unveil the dominant processes that lead to polarization in CdZnTe detectors subjected to intense x-ray irradiation.

A. Sequence of events in a polarizing detector

In order to demonstrate the observed sequence, we present the results for a subset of four simulations for a 3 mm thick detector, biased at 300 V. The voltage of the x-ray tube was set at 120 kVp, and the x-ray tube current, though held constant in each simulation, was increased from 1040 to 1280 μA in increments of 80 μA for each successive simulation. The bandgap structure used in all four simulations includes a shallow donor, a shallow acceptor, a deep donor, and an intermediate acceptor. The specific parameter values for each level are listed in Table I. Our choice of the energy levels and other defect parameters in this example is consistent with the temperature- and composition-dependent electrical resistivity and charge transport properties of fully compensated semi-insulating CdZnTe.[9] In what follows, we often imply a photon flux by referring to the x-ray tube current. This is justified by measurements under our experimental operating conditions that confirm a photon flux that is linearly proportional to the tube current[14] as predicted in the model spectrum of Eq. (11).

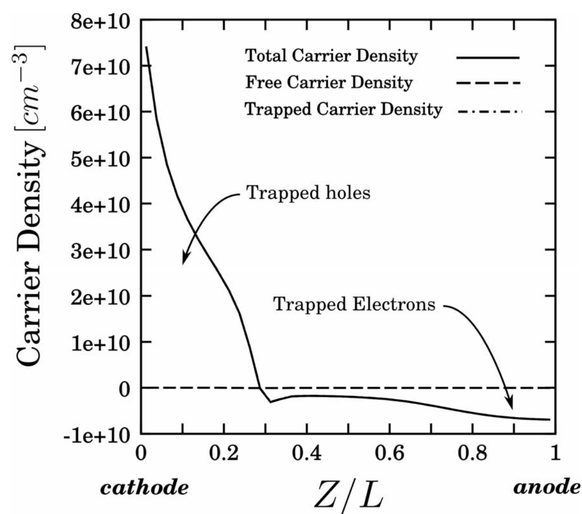

(a)Positive charge build up

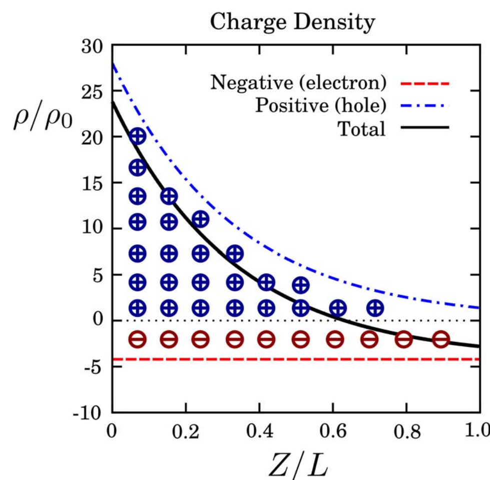

(b)Cartoon of the charge distribution

FIG. 1. (Color online) (a) The free (dashed curve), trapped (dash-dotted curve), and total (solid curve) charge densities in steady state. (b) Cartoon of the resulting total charge densities (solid curve) broken down into its positive (dash-dotted curve) and negative (dashed curve) components.

An obvious and ever-present feature in the steady state simulation data is a large concentration of positive space charge that accumulates near the cathode plane through which the photons enter the detector. An example of such a buildup of positive charge at the cathode is shown in Fig. 1(a). In this figure, we show the free (dashed curve), trapped (dot-dashed curve), and total (solid curve) charge densities in the steady state reached nearly 15 ms after the x-ray tube was turned on. The fact that the total and trapped curves are on top of one another indicates that the total charge density is dominated by the trapped space charge throughout the detector. Since the holes travel slowly and are trapped quickly, the profile of the positive space charge in Fig. 1(a) closely follows the exponential interaction profile of the x rays in

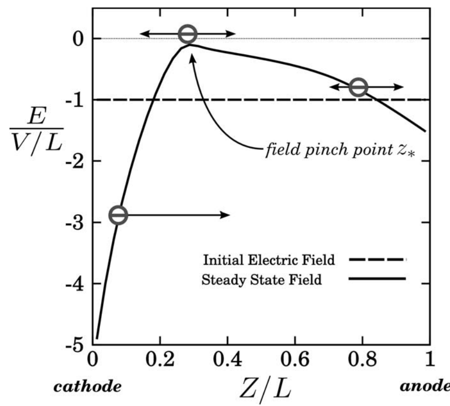

(a)Steady state electric field

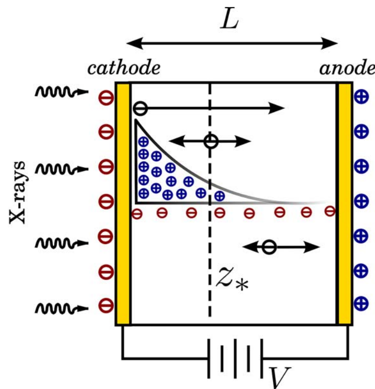

(b)Cartoon of the field strength

FIG. 2. (Color online) (a) Steady state profile of the electric field strength (solid curve) after 14.88 ms of evolution. (b) Cartoon of the charge distribution necessary to set up such a steady state for the electric field.

CdZnTe. The electrons, on the other hand, are fast and only weakly trapped, so the density of trapped electrons is smaller and more spatially uniform. An idealized cartoon of the resulting total charge density is shown in Fig. 1(b). The solid curve represents the total charge density that results from a spatially uniform density of trapped electrons (dashed line) and an exponentially decreasing density of trapped holes (dot-dashed curve).

Such a massive amount of space charge in the detector has an effect on the electric field as shown in Fig. 2(a). In this plot, we show the steady state electric field resulting from the charge density shown in Fig. 1(a). The horizontal dashed line at $e=-1$ in the plot represents the reference unperturbed value of the electric field. Note that near the cathode, the field strength in high-flux steady state is increased approximately four to five times its unperturbed value. Away from the cathode, however, there is a point at which the electric field strength is reduced to a fraction of its unperturbed value. We denote this point of reduced field strength $z=z_*$ and call it the field *pinch point*. On the anode side of the pinch point, the field strength recovers.

The development of the pinch point in the electric field is easily explained by considering a density of space charge distributed as shown in Fig. 1(b) and large enough to exert electrostatic forces equal in magnitude to those generated by the operating bias. Consider the cartoon in Fig. 2(b), where the bias voltage is depicted by a negative surface charge density on the cathode and a positive charge density on the anode. The exponential distribution of trapped holes and the uniform density of trapped electrons are also depicted as positive and negative charges. A free electron that is generated near the cathode will be accelerated toward the anode not only by the bias field but also by the electrostatic force of the positive charge it has in front of it. This results in an increased electric field near the cathode as shown in Fig. 2(a). At the pinch point, $z=z_*$, however, there is enough positive charge behind the electron to generate a force toward the cathode that very nearly balances the force on the electron in the direction of the anode due to the bias voltage. This force balance is manifested as a vanishing electric field strength at the pinch point, $z=z_*$. Electrons generated on the anode side of the pinch are once again dominated by the bias voltage, resulting in a field strength that recovers.

The pinch in the electric field has consequences for the electron transport within the crystal. Figure 3(a) shows the resulting transit times for electron clouds as a function of the depth of interaction for steady state electric fields that result from the four x-ray tube currents $I=\{1040,1120,1200,1280\}$ μA. The dotted line in this plot represents the low-flux limit of the electron transit times. In units of the transit time, it has unit value at the cathode and linearly goes to zero at the anode. As the photon flux is increased, Fig. 3(a) shows that the transit time is dramatically increased for electrons generated on the cathode side of the pinch point. In fact, at $I=1280$ μA, the transit time is nearly 60 times what it is under low-flux conditions.

At the same time the electron transit time is increased, the large concentration of both free and trapped charges near the cathode increases the local band-to-band recombination transition rate. This results in a reduced electron lifetime that is dominated by recombination processes instead of trapping to the deep donor. Figure 3(b) shows the steady state electron lifetime together with its constituents as a function of Z for the highest x-ray tube current $I=1280$ μA. The dashed line shows the uniform low-flux lifetime that is typically dominated in CdZnTe by electron trapping to the deep donor. The steady state lifetime, shown in Fig. 3(b) as a solid curve, is dominated by band-to-band recombination of free electrons with free holes. In fact, the plot shows that the lifetime has been reduced by an order of magnitude near the cathode where the transit times are the longest.

Longer transit times coupled together with a reduced lifetime for the electrons results in a lower charge collection efficiency for events that occur on the cathode side of the pinch, namely, $z<z_*$. The induction map for a parallel plate CdZnTe detector in low-flux conditions is shown as a dotted line in Fig. 4(a). The figure also shows the collection efficiency as a function of interaction depth at the same four x-ray tube currents $I=\{1040,1120,1200,1280\}$ μA. It is clear that as the photon flux is increased, the collection efficiency decreases on the cathode side of the pinch point. The reduced efficiency is due to the fact that electrons are likely to recombine while moving slowly through the pinch point in the field.

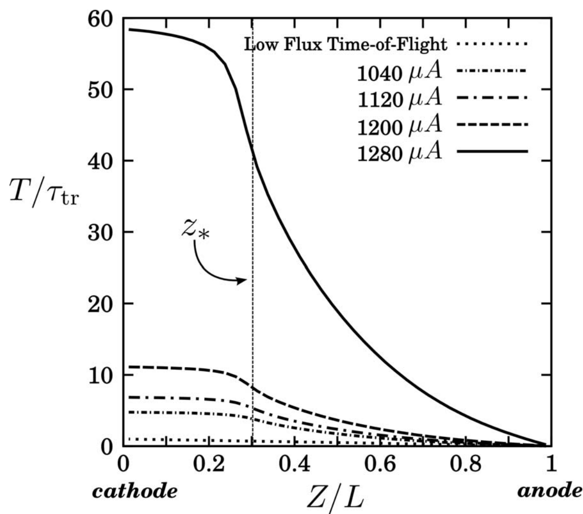

(a)Electron time-of-flight

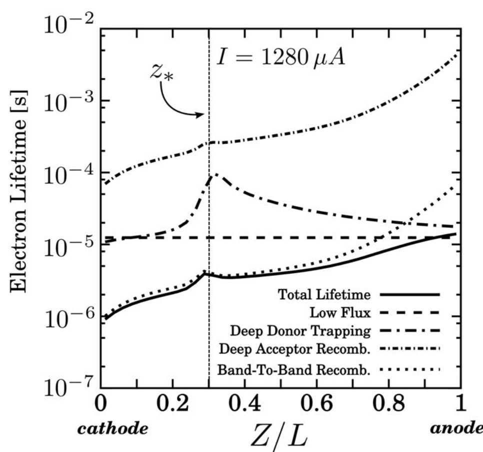

(b)Electron lifetime

FIG. 3. (a) Profiles of the resulting steady state electron time of flights at four increasing flux rates (tube currents). (b) Depthwise profiles of the steady state electron lifetime components for $I=1280$ μA. The total lifetime is shown as a solid curve.

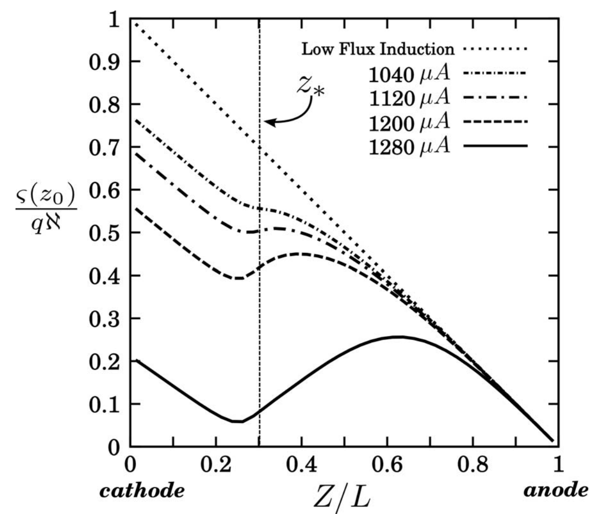

(a)Induced charge efficiency

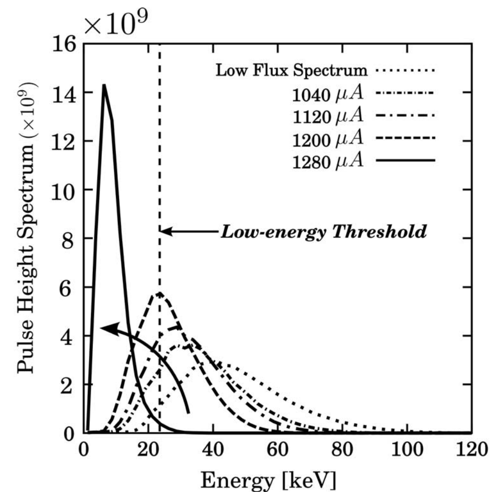

(b)Spectra in polarizing detector

FIG. 4. (a) Profiles of the resulting charge induction maps at four increasing flux rates (tube currents). (b) Resulting shift of the measured spectrum at the four increasing flux rates (tube currents).

A reduced collection efficiency, in turn, suppresses the signal amplitudes and, therefore, events are recorded at lower energies. It follows that, as the flux is increased, the entire energy spectrum shifts to the left as shown by the computed spectra in Fig. 4(b). This plot shows that as the flux increases, a larger fraction of the spectrum, and therefore counts, lies below a 25 keV low-energy counting threshold. At a high enough flux, the entire spectrum falls below the low-energy threshold as shown by the solid curve representing $I=1280$ μA in Fig. 4(b). The number of counts above the low-energy threshold for each spectra of Fig. 4(a) is shown as a solid square in Fig. 5(a). The dashed line shows the total counts in the spectrum increasing linearly with x-ray tube current. Note that as the flux is increased, there is a critical flux, denoted by Φ_γ^*, above which counts begin to decrease with an increasing current. Eventually, the detector is paralyzed, and the counts vanish entirely.

Figure 5(b) shows the actual counting response of 256 channels from a 16×16 pixel CdZnTe monolithic detector array as the photon flux is increased by increasing the x-ray tube current from 25 to 400 μA. Both the simulated counts in Fig. 5(a) and the experimentally measured counts in Fig. 5(b) initially increase with increasing flux, but at the critical flux Φ_γ^*, the counts begin to decrease with increasing photon flux. In the following section, we develop a theoretical dependence of this critical photon flux on material, detector, and operating parameters.

Finally, we point out that Fig. 4(a) shows that for the parallel plate detector simulated here, the interactions that take place for $z<z_*$ and, in particular, those very near the cathode have induced signals that benefit from the fact that the electrons are able to travel unimpeded to the pinch at $z=z_*$. This is evident in the linear rise of the induced signals of Fig. 4(a) as $z\to0$. Of course, many imaging applications do not use planar detectors but make use of monolithic detectors patterned with pixel arrays to improve image resolution. Since most of the charge in a pixelated detector is induced when the electrons are very near the anode plane (i.e.,

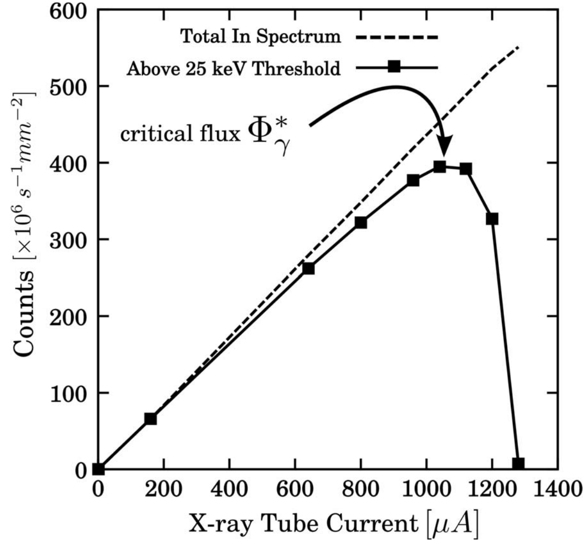

(a)Resulting counts above threshold

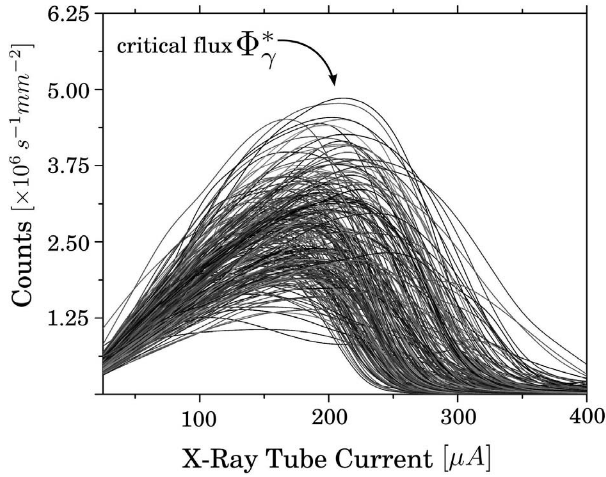

(b)Measured counts above threshold

FIG. 5. (a) Simulated counts above a 25 keV threshold as the photon flux rate (x-ray tube current) is increased. (b) Measured counts for 256 channels of a polarizing detector as the photon flux rate (tube current) is increased.

after they have passed through the pinch point), pixelated detectors will be insensitive to this early unimpeded motion of the electrons. As a consequence, pixelated detectors will be more susceptible to the above-mentioned reduced charge induction, and therefore polarization.

IV. THEORY

In the previous section, we presented a single example from a large matrix of simulations in which we solved the full set of Eqs. (7a) and (7b) subjected to an x-ray source with spectrum dn_γ/de described by Eq. (11). Not only does this example highlight the sequence of events that take place in a polarizing detector but it also demonstrates the dominant role played by the hole transport in the polarization sequence. Specifically, it is the large buildup of positive charge (i.e., number density of both free and trapped holes) within the detector that begins the sequence by creating a pinch point in the electric field as shown in Fig. 2(a). In fact, in the absence of a pinch point, the electric field strength is never low enough to sufficiently reduce the electron transport to a level that shifts the spectrum below the low-energy threshold.

In this section, we exploit the dominant role of the hole dynamics to develop an analytic expression that approximately describes the dependence of the maximum sustainable flux on critical material, operating, and detector design parameters. The analysis we present assumes that polarization is the end result of the creation of a pinch point in the electric field, and the method can be summarized as follows:

(1) The amount of charge, denoted by Q^*, that is necessary to collapse the electric field at a pinch point is calculated.

(2) The time dependence, $Q(T)$, of the buildup of positive charge density within the detector is calculated.

(3) Polarization results when the time-asymptotic limit (i.e., steady state value) of the buildup of positive charge exceeds that necessary to collapse the electric field at the pinch point. Mathematically, this is expressed as $\lim_{T\to\infty} Q(T)=Q^*$.

The result of the third step, as we will show, is the desired functional dependence of the maximum sustainable flux (i.e., critical flux Φ_γ^*) on device design and operating parameters.

A. Necessary positive charge

We begin by considering a photon source with uniform flux Φ_γ describing the number of photons per $cm^2\, s^1$ that intersect the cathode surface of the detector at right angles. The source is assumed to be monoenergetic with energy taken as the mean value of the x-ray spectrum of Eq. (11) and denoted by $\bar{E}_\gamma$. The generation rate of electron-hole pairs within the detector, therefore, is exponentially distributed and has the form

$$\Psi(Z) = \Phi_\gamma \frac{\bar{E}_\gamma}{\epsilon_{czt}} \frac{1}{\Lambda} e^{-Z/\Lambda}, \tag{12}$$

where ϵ_{czt} is the pair creation energy for CdZnTe, and $\Lambda \to \Lambda(\bar{E}_\gamma)=\mu(\bar{E}_\gamma)^{-1}$ is the characteristic length scale that a photon travels before interacting in CdZnTe (i.e., inverse of the *linear attenuation coefficient*). In order to simplify notation, we define $\Psi_0=\bar{E}_\gamma\Phi_\gamma/\epsilon_{czt}$ that represents the number of electron-hole pairs being created per $cm^2\, s^1$.

We have shown that since the holes are slow moving and rapidly trapped, the positive buildup of charge due to both free and trapped holes can be approximated by the exponential form of the charge generation in Eq. (12), which was shown as a dot-dashed curve in Fig. 1(b). Recall that the electrons, on the other hand, are fast and trapped much less frequently, so the negative charge density present due to electrons must be approximated by a small and spatially uniform charge density as shown in the cartoon of Fig. 1(b). Therefore, the total charge density built up after T seconds can be approximated by

$$\rho(Z) = qT\Psi_0 \frac{1}{\Lambda} e^{-Z/\Lambda} - qT\Psi_0 \delta/L = \rho_0 \left(\frac{1}{\Lambda} e^{-Z/\Lambda} - \delta/L \right), \tag{13}$$

where δ is a small nondimensional parameter representing the relative number of trapped electrons to holes, and we have defined $\rho_0 = qT\Psi_0$ for convenience of the notation. This approximation to the steady state charge density is shown as a solid curve in the cartoon of Fig. 1(b).

In order to find the resulting electric field, we turn to the Poisson problem which can be written as

$$\frac{d^2\phi}{dZ^2} = -\frac{\rho_0}{\epsilon_0}\left(\frac{1}{\Lambda} e^{-Z/\Lambda} - \delta/L \right), \tag{14a}$$

$$\phi(Z=0) = -\mathcal{V}, \tag{14b}$$

$$\phi(Z=L) = 0. \tag{14c}$$

Integrating Eq. (14a) twice and applying the boundary conditions (14b) and (14c) yields a solution for the electric potential within the detector,

$$\phi(Z) = (Z/L - 1)\left[\mathcal{V} + \frac{\rho_0}{\epsilon_0}(\delta Z - \Lambda) \right] - \Lambda \frac{\rho_0}{\epsilon_0}\left[e^{Z/\Lambda} - \frac{Z}{L} e^{-L/\Lambda} \right]. \tag{15}$$

The electric field immediately follows as the negative gradient of ϕ,

$$E(Z) = -\frac{d}{dZ}\phi(Z) = -\frac{\mathcal{V}}{L}\left\{ 1 - \frac{\rho_0 L}{\epsilon_0 \mathcal{V}}\left[\frac{\Lambda}{L} + \delta\left(1 - \frac{2Z}{L} \right) - e^{-Z/\Lambda} - \frac{\Lambda}{L} e^{-L/\Lambda} \right] \right\}. \tag{16}$$

Now that we have the electric field as a function of Z, we can compute the location of the pinch point that will be denoted by Z^*. Since the pinch point represents a global minimum of the field strength $\|E(Z)\|$, Z^* is located where the derivative of the electric field strength vanishes,

$$\left.\frac{dE}{dZ}\right|_{Z=Z^*} = \frac{\rho_0}{\epsilon_0}\left(\frac{2\delta}{L} - \frac{1}{\Lambda} e^{-Z^*/\Lambda} \right) = 0. \tag{17}$$

This can easily be solved for the location of the pinch point,

$$Z^* = -\Lambda \ln(2\delta\Lambda/L), \tag{18}$$

which can be substituted back into Eq. (16) to find the strength of the electric field at the pinch point. We point out that having an expression for the strength of the electric field at Z^* takes us nearly to the goal of this section, which is to find the amount of charge necessary to collapse the field at the pinch point [i.e., where $E(Z^*) \to 0$]. Prior to writing the resulting expression for the field strength, we note that it can be further simplified using the fact that $\delta \ll 1$ since trapping is weak for electrons when compared to that of holes. Therefore, substituting Eq. (18) into Eq. (16), taking the limit as δ vanishes, and setting the result to zero yields

$$\lim_{\delta \to 0} E(Z^*) = -\frac{\mathcal{V}}{L}\left\{ 1 - \frac{\rho_0^* \Lambda}{\epsilon_0 \mathcal{V}}(1 - e^{-L/\Lambda}) \right\} = 0, \tag{19}$$

which defines the minimum charge density, denoted ρ_0^*, that is necessary to collapse the field at the pinch point. Solving this equation for ρ_0^* gives

$$\rho_0^* = \frac{\epsilon_0 \mathcal{V}}{\Lambda \beta}, \tag{20}$$

where we have defined $\beta = [1 - \exp(-L/\Lambda)]$. Recall that ρ_0 represents the amount of charge per unit area in the detector and that the volumetric density of charge is exponentially distributed in the Z direction, so we can express the total charge in the detector as

$$Q = A\rho_0 \int_0^L \frac{1}{\Lambda} e^{-Z/\Lambda} dZ = A\rho_0 \beta. \tag{21}$$

Therefore, we can use Eq. (21) to express the minimum total charge necessary to collapse the electric field at the pinch point,

$$Q^* = A \frac{\epsilon_0 \mathcal{V}}{\Lambda}. \tag{22}$$

This equation contains the relationship that we have been seeking. As one may expect, Q^* is proportional to the applied bias voltage since it clearly takes more charge to collapse the stronger field generated by a larger applied bias voltage.

B. Time dependence of positive charge buildup

So far, we have developed an approximation to the minimum amount of charge necessary to begin the process of polarization (i.e., collapse the field at the pinch point). In this section, we derive an approximation to the time evolution of the positive charge buildup in the detector. Once again, we turn to the results of simulation that show that there are two dominant dynamics that govern the time evolution of the charge that builds up in the detector:

(1) positive charge is increased due to the x-ray source generating holes and

(2) positive charge is decreased due to an outgoing flux of holes.

Since the levels of trapped holes start off quite low, at the moment the x-ray source is turned on, the increase in charge due to generation dominates. This causes a buildup of positive charge density. However, as the holes build up near the cathode, more and more of them exit the detector once they are detrapped. Consequently, there is an asymptotic limit to the total positive charge in the detector.

We begin by calculating the charge buildup with a simple rate equation in Sec. IV B 1. Though this solution is shown to be useful at photon energies for which the detector fully absorbs the photons (i.e., for $\Lambda \ll L$), we find that we must turn to a more sophisticated analysis to accurately describe the charge buildup for high-energy photons. The more accurate analysis is presented here in Sec. IV B 2 and is based on

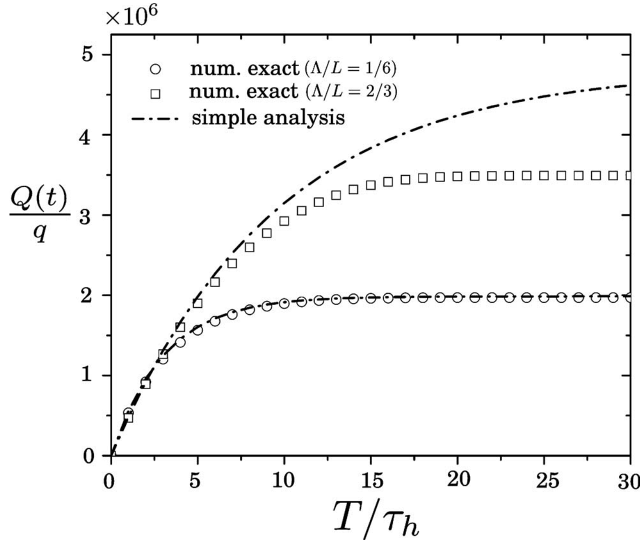

FIG. 6. Charge buildup $Q(T)$ predicted by simple analysis (dot-dashed curves) at two values of the parameter Λ, namely, Λ/L={1/6,2/3}. Full numerical solution is shown as circles for Λ/L=1/6, and squares for Λ/L=2/3.

a multiple scale technique described in detail in Ref. 7.

1. Simple method

To calculate this time-asymptotic limit, we begin by writing down the change in total charge during any time interval ΔT,

$$\Delta Q = Aq\Psi_0\Delta T\beta - (v_h\Delta T)A\rho_0/\Lambda = Aq\Psi_0\Delta T\beta - (v_h\Delta T)\frac{Q}{\Lambda\beta}, \tag{23}$$

where, in the second equality, we have used Eq. (21). The first term on the right hand side of Eq. (23) represents the increase in charge due to the generation source, and the second term represents the loss of charge due to the flux of holes out of the detector. Note that the holes are assumed to be traveling at speed v_h, which will be discussed in detail shortly. Taking the infinitesimal limit $\Delta T \to 0$ yields the rate equation

$$\frac{dQ(T)}{dT} = qA\Psi_0\beta - v_h\frac{Q(T)}{\Lambda\beta}. \tag{24}$$

This differential equation has the simple solution

$$Q(T) = \frac{Aq\Psi_0\beta^2\Lambda}{v_h}\left[1 - \exp\left(-\frac{v_h}{\Lambda\beta}T\right)\right] \tag{25}$$

in time. Equation (25) is shown as dot-dashed curves in Fig. 6 for both high-, and low-energy photons represented by two values of the parameter Λ, namely, Λ/L={1/6,2/3}. The solution has the characteristics we expect; the charge initially grows quickly and then exponentially asymptotes to a value that is proportional to Ψ_0 and inversely proportional to the velocity of the holes v_h. Figure 6 also shows a full numerical solution for this example as circles for low-energy photons with Λ/L=1/6, and squares for high-energy photons with Λ/L=2/3. It is clear that when the photons are fully absorbed by the detector, Eq. (25) does quite well. However, when photons are only partially absorbed (i.e., the photon energy is large enough so that $\Lambda/L \sim 1$), this simple solution overestimates the charge buildup with a large error.

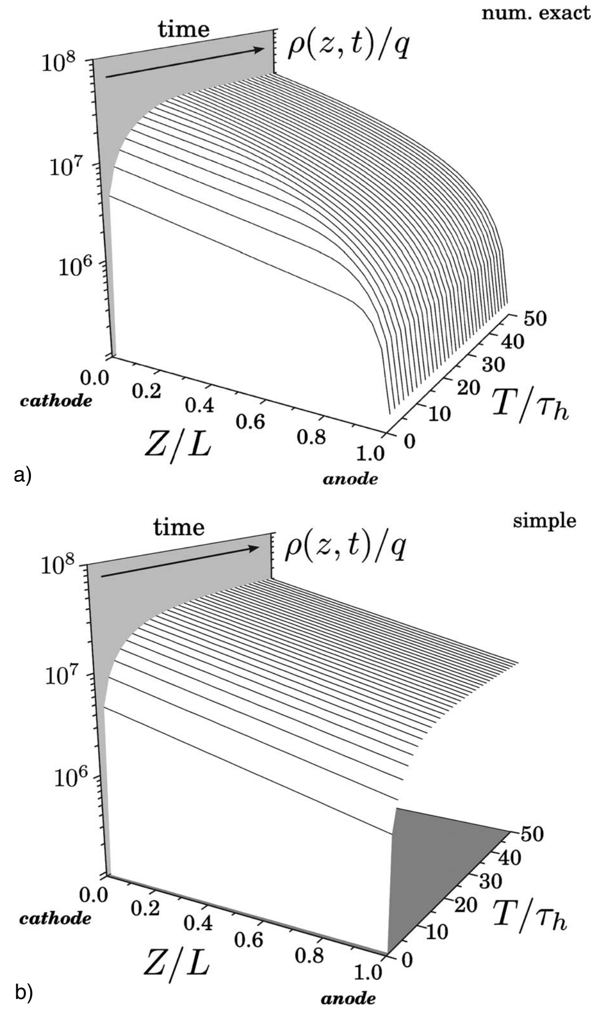

FIG. 7. Space-time evolution of the buildup of positive charge density. The parameter $\Lambda(e_\gamma)/L$=2/3 so that there are penetrating photons.

The reason for this overestimation is clear if we point out that this simple analysis has only assumed an exponentially distributed density of holes and does not take into consideration the fact that this distribution will change as the holes move away from the anode plane. Figure 7 compares the space-time evolution of the charge density for Λ/L=2/3 so that photons are deposited throughout the detector thickness. The full numerical solution is shown in Fig. 7(a), while the simple analytical result is shown in Fig. 7(b). Note that the overestimation of charge is due to the error near the anode plane at z=1. The simple analytical solution neglects the fact that holes are moving away from the anode plane, thereby reducing the charge density there.

2. Multiple scale solution

Figures 6 and 7 show that the simple analytical solution in Eq. (25) does not accurately predict the value of the positive

charge within the detector as $T \to \infty$ when the photon energy is high enough that there are interactions throughout the detector. In addition to this, it is troubling that the simple solution is not capable of decomposing the positive charge into free and trapped carrier constituents, P and $\hat{P}$, respectively. Therefore, in order to obtain a more accurate and complete description of the charge buildup within the detector, we turn to a multiple scale perturbation technique whose details are developed in Ref. 7 and briefly summarized here.

We begin by reducing the full set of Eqs. (7a) and (7b) to the relevant system of partial differential equations that describe the transport, trapping, and subsequent detrapping of holes in the presence of a single, dominant hole trap. The resulting scaled system of equations can be written as

$$\partial_t p + \epsilon \partial_z (ep) = - p + \eta \frac{\tau_h}{\tau_D} \hat{p} + \psi, \tag{26a}$$

$$\partial_t \hat{p} = \frac{1}{\eta} p - \frac{\tau_h}{\tau_D} \hat{p}, \tag{26b}$$

$$\partial_z^2 \phi = - \gamma (p + \eta \hat{p}), \quad e = - \partial_z \phi, \tag{26c}$$

where we have used Eqs. (5a) and (5b) to scale the concentrations, and ψ is the nondimensional version of the hole generation source in Eq. (12) with form

$$\psi = \psi_0 \frac{1}{\lambda} e^{-z/\lambda}. \tag{27}$$

In both system (26a)–(26c) and Eq. (27), we have introduced $\lambda = \Lambda / L$, as well as the nondimensional source of holes $\psi_0 = (\tau_h \Phi_\gamma E_\gamma) / (P_0 L \epsilon_{czt})$. The parameter in front of the drift term of Eq. (26a) is a small parameter $\epsilon = \tau_h \mu_h \mathcal{V} / L^2 \ll 1$, representing the fraction of the detector thickness, on average, that a hole travels before trapping. The hole trapping time τ_h is defined in terms of the trapping rate $\Lambda^1_{\downarrow:A}$, so that

$$\tau_h = (\Lambda^1_{\downarrow:A})^{-1} \approx \frac{1}{\sigma_A^1 \theta \mathcal{P}^1}, \tag{28}$$

where we have assumed the ionized fraction of the acceptor to be constant. In Eqs. (26a)–(26c), we have also defined the hole detrapping time τ_D, which is defined in terms of $\Lambda^1_{\uparrow:A}$ as

$$\tau_D = (\Lambda^1_{\uparrow:A})^{-1} = \frac{1}{\nu_A^1} \exp\left(\frac{E_A^1}{kT} \right), \tag{29}$$

where ν_A^1 is the escape frequency typically set by the principal of detailed balance for the system in steady state or in thermal equilibrium.

The multiple scale technique takes advantage of the fact that there are two distinct time scales in this problem. The first is a fast time scale defined by the rapid trapping of holes and denoted by $t_1 = t$. The second is a slow time scale defined by the transit time of the holes and is denoted by $t_2 = \epsilon t$. These time scales are considered independent and define a two-scale perturbation expansion for the free and trapped hole concentrations, as well as the electric potential,

$$p(z,t) = \frac{1}{\epsilon} p_{-1}(z,t_1,t_2) + p_0(z,t_1,t_2) + \epsilon p_1(z,t_1,t_2) + O(\epsilon^2), \tag{30a}$$

$$\hat{p}(z,t) = \frac{1}{\epsilon} \hat{p}_{-1}(z,t_1,t_2) + \hat{p}_0(z,t_1,t_2) + \epsilon \hat{p}_1(z,t_1,t_2) + O(\epsilon^2), \tag{30b}$$

$$\phi(z,t) = \phi_0(z,t_1,t_2) + \epsilon \phi_1(z,t_1,t_2) + O(\epsilon^2). \tag{30c}$$

We point out that the dominant terms of both the free and trapped hole concentrations are not assumed $O(1)$, but taken to be $O(\frac{1}{\epsilon})$. The reason for this is that the small parameter ϵ is the nondimensional speed at which the holes travel toward the cathode plane [e.g., see the drift term of Eq. (26a)]. It has been shown that solutions to drift equations with a continuous source such as that in Eq. (26a) depend inversely on the nondimensional carrier speed ϵ.[7] Such a dependence on the inverse of the speed is exhibited in Eq. (25) previously found by the simple analysis. It follows, therefore, that the dominant terms of expansions (30a)–(30c) should be chosen to be inversely proportional to the small parameter ϵ.

The multiple scale solution process proceeds by solving successively higher orders of the equations that result from substituting expansions (30a)–(30c) into Eqs. (26a)–(26c). As the problem is solved at a particular order of the small parameter ϵ, the degree of freedom that comes from having two independent time scales is used to eliminate secular growth at the next order, providing accurate and stable perturbation solutions over long time scales.[15] Details of the multiple scale solution of Eqs. (26a)–(26c) with ψ given by Eq. (27) are presented elsewhere,[7] so here, we simply present the dominant solutions for p and $\hat{p}$,

$$p(z,t) = \psi_0 \frac{1}{\nu\epsilon} e^{-z/\lambda} [1 - e^{-(\nu\epsilon/\lambda)t} H(\theta^-) - e^{-(1/\lambda)(1-z)} H(-\theta^-)] \times [\nu + (1-\nu) e^{-t/(1-\nu)}] + O(1), \tag{31a}$$

$$\hat{p}(z,t) = \psi_0 \frac{1-\nu}{\eta\nu\epsilon} e^{-z/\lambda} [1 - e^{-(\nu\epsilon/\lambda)t} H(\theta^-) - e^{-(1/\lambda)(1-z)} H(-\theta^-)] \times [1 - e^{-t/(1-\nu)}] + O(1), \tag{31b}$$

where $H(x)$ is the Heaviside step function, and we have introduced the characteristic variable $\theta^- = 1 - z - \epsilon \nu t$, with the

nondimensional parameter ν defined by $\nu=\tau_h/(\tau_h+\tau_D)$. This characteristic variable naturally emerges from the multiple scale solution process and further defines the reduced effective speed of the holes,

$$v_{\mathrm{eff}} = \frac{L}{\tau_h}\epsilon\frac{\tau_h}{\tau_h+\tau_D} = \frac{\tau_h}{\tau_h+\tau_D}\mu_h E, \tag{32}$$

first found by Zanio *et al.*[16] and recently derived by the authors using multiple scales.[7] This reduced effective speed of the holes is a result of the *stop and go* process that results from multiple cycles of trapping and detrapping during hole transit.

Having found solutions (31a) and (31b) representing space-time functions for the free and trapped concentration of holes, respectively, we compute the total charge density by simply summing them together. The result is written in terms of physical space and time variables (Z,T) in the form

$$\rho(Z,T) = qP_0[p(Z,T) + \eta\hat{p}(Z,T)] = q\frac{\Phi_\gamma E_\gamma}{v_{\mathrm{eff}}\epsilon_{czt}}e^{-Z/\Lambda}\begin{cases}1-\exp\left(-\dfrac{v_{\mathrm{eff}}}{\Lambda}T\right), & T\le\dfrac{L-Z}{v_{\mathrm{eff}}}\\ 1-\exp\left(-\dfrac{L-Z}{\Lambda}\right), & T>\dfrac{L-Z}{v_{\mathrm{eff}}},\end{cases} \tag{33}$$

where we have used our definition of $\psi_0=(\tau_h\Phi_\gamma E_\gamma)/(P_0L\epsilon_{czt})$. This space-time dependence of the buildup of charge density within the detector is compared to the full numerical solution in Fig. 8 for $\Lambda/L=2/3$. The full numerical solution is shown in Fig. 8(a), and Eq. (33) is plotted in Fig. 8(b). Note that the multiple scale solution matches the numerical solution very well and has captured the fact that the hole density is lower near the anode plane at $Z=L$.

A simple integral of the charge density over the detector thickness gives what we seek in this section, namely, the time dependence of the buildup of positive charge within the detector,

$$Q(T) = q\frac{A\Phi_\gamma E_\gamma}{v_{\mathrm{eff}}\epsilon_{czt}}\Lambda\begin{cases}1-\exp\left(-\dfrac{v_{\mathrm{eff}}}{\Lambda}T\right)-\dfrac{v_{\mathrm{eff}}}{\Lambda}T\exp\left(-\dfrac{L}{\Lambda}\right), & T\le L/v_{\mathrm{eff}}\\ 1-\left(1+\dfrac{L}{\Lambda}\right)\exp\left(-\dfrac{L}{\Lambda}\right), & T>L/v_{\mathrm{eff}}.\end{cases} \tag{34}$$

This analytical approximation is shown as a solid curve in Fig. 9, where it is compared with a full numerical solution shown as circles at the lower photon energy with $\Lambda/L=1/6$ and squares at the higher energy with $\Lambda/L=2/3$. The charge buildup predicted by the simple method is also shown as a dot-dashed curve for comparison of the two analytical solutions. It is clear from Fig. 9 that $Q(T)$ derived using the multiple scale perturbation technique accurately predicts the charge buildup for both low- and high-energy photons.

As a final note, recall that the simple solution method gave no indication whether the excess charge was made of free or trapped holes. The multiple scale solutions (31a) and (31b), on the other hand, clearly distinguish the constituents of the positive charge. Comparing Eq. (33) with Eq. (31a), it is clear that the time-asymptotic fraction of free holes that contribute to Q is given by $\nu=\tau_h/(\tau_h+\tau_D)$ and the fraction of trapped holes is given by $1-\nu=\tau_D/(\tau_h+\tau_D)$. In real crystals of CdZnTe, however, the acceptor level responsible for the hole trapping is a deep level,[17] so that $\tau_D\gg\tau_h$ and $\nu\ll 1$, meaning that the positive charge is predominantly made of trapped space charge.

C. Maximum sustainable photon flux

So far, we have derived Q^* in Eq. (22), approximating the minimum charge necessary to create the pinch point in the electric field that is necessary to polarize a detector. In Eq. (34), we used a multiple scale perturbation technique to derive $Q(T)$ describing the time dependence of the buildup of positive charge in a detector subjected to a photon flux Φ_γ. We are now in a position to derive the maximum sustainable flux above which a detector will polarize, and we denote this *critical flux* by Φ_γ^*. The critical flux we seek simply comes from equating the time-asymptotic limit of the total charge $Q(T)$ to that needed for polarization, Q^*, or

$$\lim_{t\to\infty} Q(t) = Q^*. \tag{35}$$

Using Eqs. (22) and (34), the above equality can be rewritten as

$$\frac{q\bar{E}_\gamma\Phi_\gamma^*\Lambda}{\epsilon_{czt}v_{\mathrm{eff}}}\left(\beta-\frac{L}{\Lambda}e^{-L/\Lambda}\right) = \frac{\epsilon_0\mathcal{V}}{\Lambda}, \tag{36}$$

where we have used the fact that we had previously defined $\beta=1-\exp(-L/\Lambda)$. Finally, we use Eq. (32) to substitute for v_{eff} and solve for Φ_γ^* to get

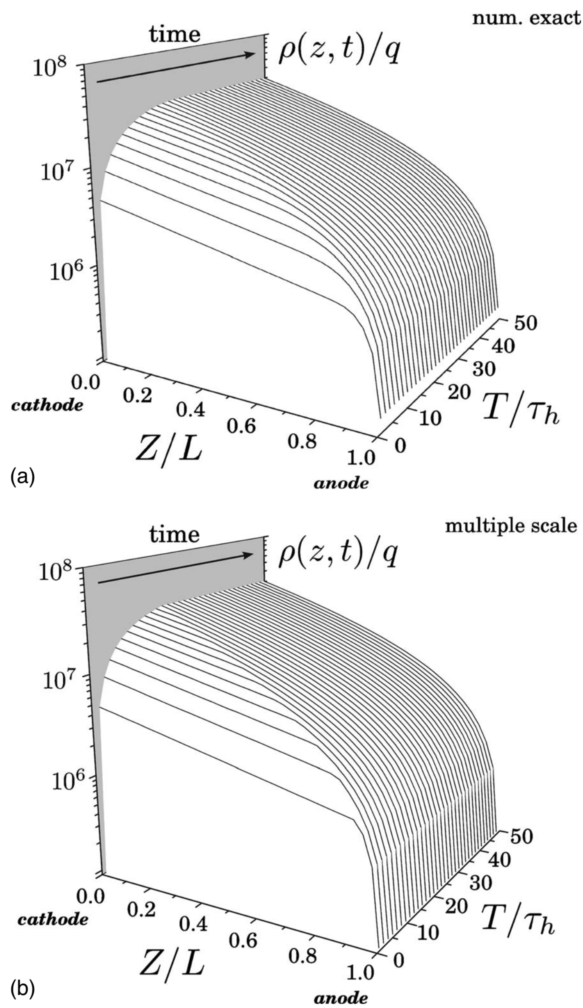

FIG. 8. Space-time evolution of the buildup of positive charge density. The parameter $\Lambda(e_\gamma)/L=2/3$, so that there are penetrating photons.

$$\Phi_\gamma^* = \frac{\epsilon_0\epsilon_{czt}\mathcal{V}^2}{qL\bar{E}_\gamma\Lambda^2}\left(\beta - \frac{L}{\Lambda}e^{-L/\Lambda}\right)^{-1}\frac{\mu_h\tau_h}{\tau_h+\tau_D}. \quad (37)$$

This equation expresses the desired relationship between the maximum sustainable flux and the critical material, operating, and detector design parameters for the CdZnTe device.

We point out that using $Q(T)$ in Eq. (25) derived by the simple rate equation of Sec. IV B 1 in the limit on the left side of Eq. (35) yields an approximation to the maximum sustainable flux of the form

$$\Phi_\gamma^* = \frac{\epsilon_0\epsilon_{czt}\mathcal{V}^2}{qL\bar{E}_\gamma(\Lambda\beta)^2}\frac{\mu_h\tau_h}{\tau_h+\tau_D}, \quad (38)$$

which was previously reported by the authors.[18,19] Note that for low photon energies such that $\Lambda/L \ll 1$ with few photons interacting deep in the detector, we have $\beta \to 1$, and Eqs. (37) and (38) become equivalent. However, for energies such that there are interactions throughout the detector, as one would expect from the plot in Fig. 9 in Sec. IV B 2, the expression for Φ_γ^* in Eq. (37) is much more accurate.

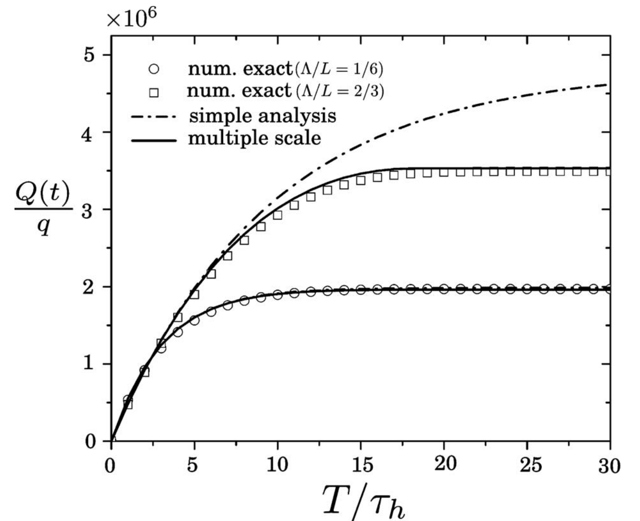

FIG. 9. Charge buildup $Q(T)$ predicted by multiple scale analysis (solid curves) and simple analysis (dot-dashed curves). Full numerical solution is shown as circles for $\Lambda/L=1/6$ and squares for $\Lambda/L=2/3$.

The expression for Φ_γ^* in Eq. (37) provides a theoretical foundation upon which critical material, operating, and detector parameters can be chosen when designing a semiconductor device applied to high-flux x-ray imaging applications. In the following subsections, we highlight the functional dependence of Φ_γ^* on a few such design parameters and validate them using experimentally measured data.

1. Bias voltage dependence

The quadratic dependence of the critical flux on the operating bias voltage $\mathcal{V}$ is clear in Eq. (37). That is, doubling the bias will increase the maximum sustainable flux by a factor of 4 under conditions where all other parameters are held constant. Figure 10(a) shows a surface plot of the critical flux [Eq. (37)] as a function of the hole mobility-lifetime product and the bias voltage. The linear dependence of Φ_γ^* on $\mu_h\tau_h$, as well as its quadratic dependence on $\mathcal{V}$, is shown in this plot for a 3 mm thick detector at room temperature and $E_A = 0.73$ eV. The mean photon energy was assumed to be 60 keV, from which it follows that $\Lambda/L \approx 0.1$. Figure 10(b) shows the same dependencies as a contour map.

In order to experimentally validate the quadratic bias dependence, we selected five 3 mm thick 16×16 pixel CdZnTe monolithic detector arrays with low hole transport that demonstrated polarizing characteristics. Details of the fabrication process for these devices have been reported in Refs. 14 and 19. Each detector was temperature stabilized and subjected to a 120 kVp x-ray source, for which the current was ramped from 10 to 400 μA in increments of 5 μA. At each value of the tube current (photon flux), the 256 channels of count values were averaged and read out. This process was repeated for five voltages $\mathcal{V} \in \{300,400,500,600,700\}$ V. All five detectors gave similar results, and we show the resulting count curves for a single detector in Fig. 11(a). At each bias voltage, the critical flux was determined by fitting such curves to pick off the tube

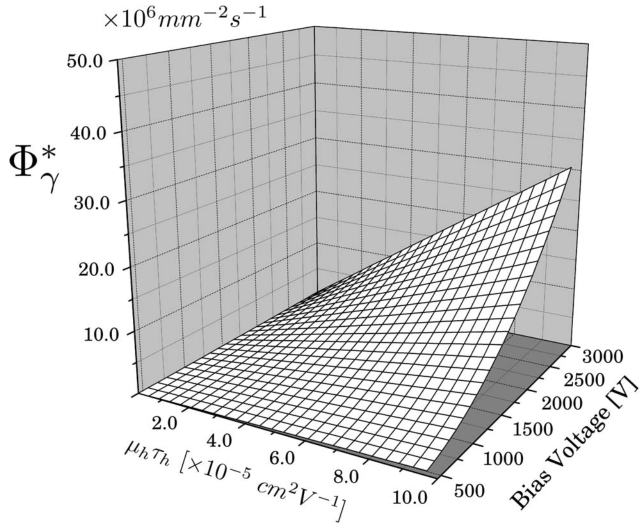

(a)Surface Plot

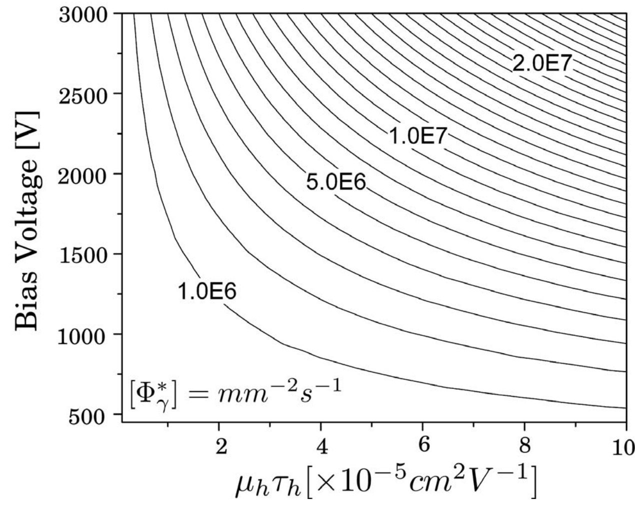

(b)Φ^*_γ = const. contours

FIG. 10. (a) Surface and (b) contour plots of the dependence of Φ^*_γ on bias voltage.

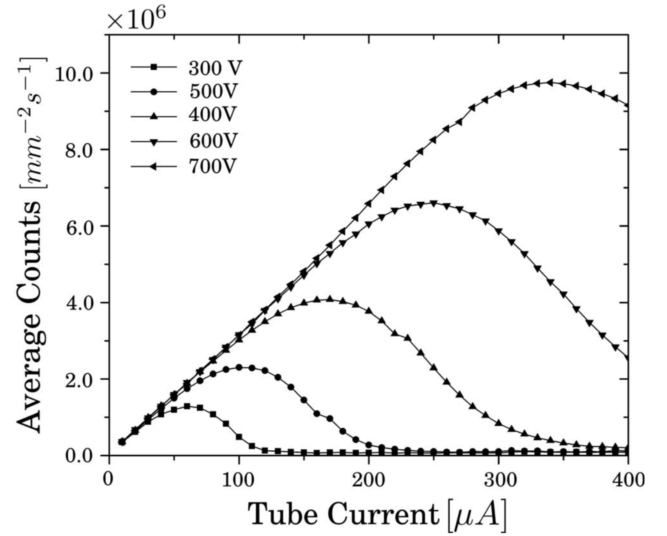

(a)Voltage dependence of counts

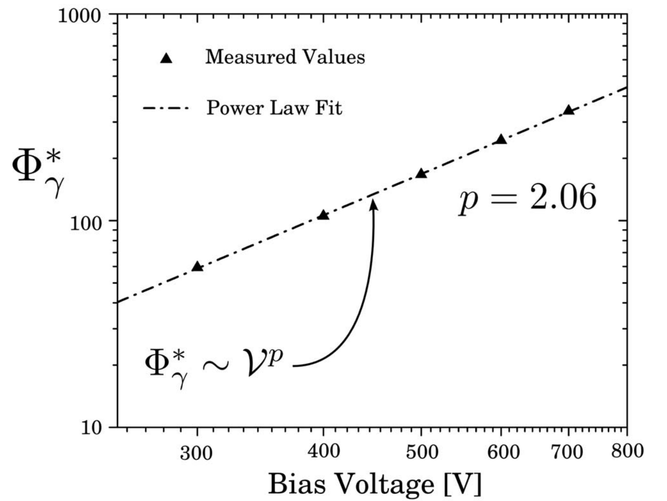

(b)maximum sustained flux

FIG. 11. Experimentally measured dependence of the maximum sustainable flux on bias voltage.

current at which the maximum count values occurred [e.g., see plots in Figs. 5(a) and 5(b)]. A log-log plot of the measured values for the same detector is shown in Fig. 11(b) (solid triangles), together with a power law fit to the data. The result of the fit shows that the data are best represented by a power law with power $p=2.06$. This is precisely the quadratic dependence predicted by Eq. (37).

2. Temperature dependence

The dependence of the critical flux on temperature comes through the hole detrapping time τ_D that resides in the denominator of Eq. (37). Specifically, the temperature dependence is evident in the definition of Eq. (29), so that

$$\Phi^*_\gamma \sim \exp\left(-\frac{E_A}{k\mathcal{T}}\right), \tag{39}$$

where E_A is the ionization energy of the dominant trap responsible for the hole trapping. Therefore, there is an exponential dependence of the maximum sustainable flux on the operating temperature of the detector. Figure 12 shows a surface and contour plot of Φ^*_γ as a function of both the hole mobility-lifetime product and the temperature. The strong dependence of the critical flux on temperature is evident in the surface plot of Fig. 12(a).

In order to experimentally validate this exponential temperature dependence, we have once again used the same set of detectors described in Sec. IV C 1. In this set of experiments, however, we have held the bias voltage fixed at 900 V and varied the temperature in the range $\mathcal{T} \in \{15,20,25,30,35,40,45\}$ C. The measured values for Φ^*_γ at each temperature for the same detector used in Fig. 11 are plotted in Fig. 13 (solid triangles), together with an exponential fit (dot-dashed curve). The data are best fitted with an exponential curve with $E_A=0.76$ eV, which corresponds to a deep acceptor level at the middle of the bandgap, as one would expect.

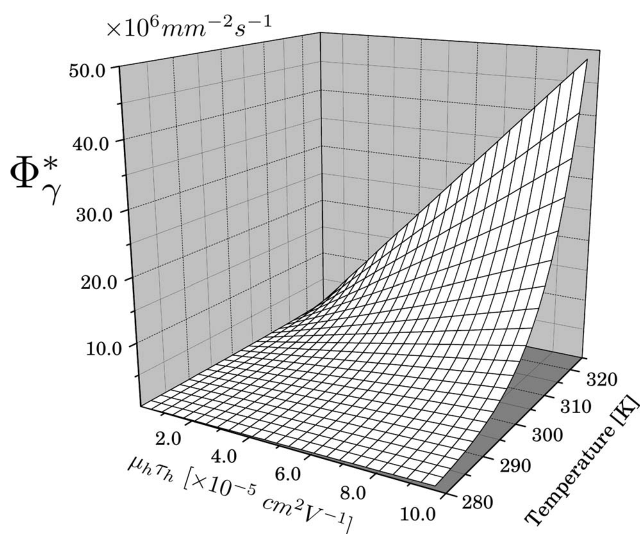

(a)Surface Plot

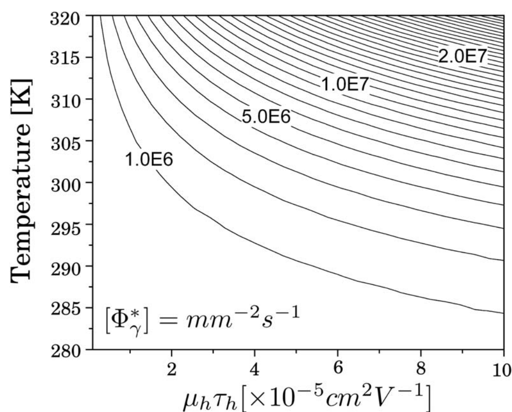

(b)$\Phi_\gamma^* =$ const. contours

FIG. 12. (a) Surface and (b) contour plots of the temperature dependence of Φ_γ^*.

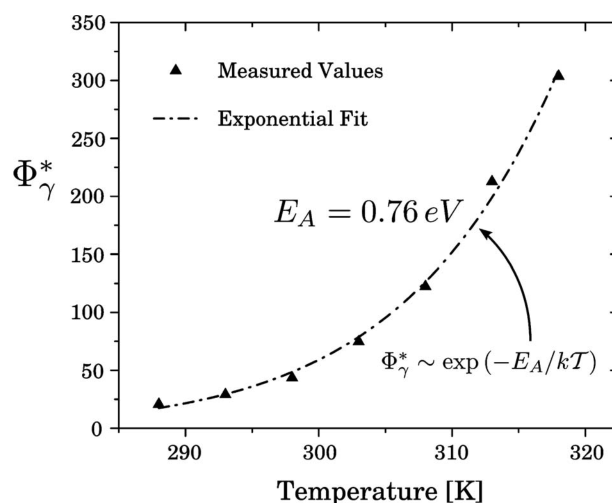

FIG. 13. Experimentally measured temperature dependence of the critical flux. Measured values are shown as solid triangles, while an exponential fit to the data is shown as a dot-dashed curve. The energy level of the deep acceptor responsible for the hole trapping that creates the best fit is E_A=0.76 eV, as shown in the plot.

V. CONCLUSION

We have developed a general mathematical model for the defect structure in the bandgap of CdZnTe that is applicable to any wide-bandgap semiconductor and capable of describing carrier transport and defect transition dynamics in the presence of a high-flux x-ray source. The model allows for an arbitrary number of both donor and acceptor defects within the crystal. The resulting nonlinear system of balance laws have been numerically solved using flux-conservative wave propagation algorithms developed for conservation laws with spatially varying flux functions.[4,5] The code developed has been applied to a large matrix of simulations, in which a parallel plate detector has been subjected to a flux of photons emanating from an x-ray tube. The simulation data have highlighted the dominant hole dynamics that trigger a sequence of events that ultimately result in a reduced charge collection efficiency of the electrons. This reduced efficiency causes count spectra to shift to lower energies, meaning that fewer counts are above the low-energy counting threshold. As the flux is raised above a critical value, denoted here by Φ_γ^*, counts begin to decrease as the flux is increased, ultimately leading to a polarized detector.

The dominant role of the transport of slowly moving holes has been exploited with the application of multiple scale perturbation techniques[7] to derive an analytic expression describing Φ_γ^* as a function of critical material, operational, and detector design parameters. The functional dependencies of the maximum sustainable flux on bias voltage and temperature have been validated experimentally using 16×16 pixel CdZnTe monolithic detector arrays subjected to a high-flux 120 kVp x-ray source.

ACKNOWLEDGMENTS

The authors acknowledge fruitful discussions with Michael Prokesch, Stephen Soldner, and David Rundle and are grateful to Jesse Graves and Bradley Hughs for the automation of experimental data collection. This work has been supported in part by the U.S. Army Armament Research, Development, and Engineering Center (ARDEC) under Contract No. DAAE 30-03-C-1171.

*dbale@ii-vi.com

[1] A. Jahnke and R. Matz, Med. Phys. **26**, 38 (1999).
[2] D. Vartsky, M. Goldberg, Y. Eisen, Y. Shamai, R. Dukhan, P. Siffert, J. M. Koebel, R. Regal, and J. Gerber, Nucl. Instrum. Methods Phys. Res. A **263**, 457 (1988).
[3] Y. Du, J. LeBlanc, G. E. Possin, B. D. Yanoff, and S. Bogdanovich, IEEE Trans. Nucl. Sci. **50**, 1031 (2003).
[4] D. S. Bale, Ph.D. thesis, University of Washington, 2002.
[5] D. S. Bale, R. J. LeVeque, S. Mitran, and J. A. Rossmanith, SIAM J. Sci. Comput. (USA) **24**, 955 (2002).
[6] R. J. LeVeque, J. Comput. Phys. **131**, 327 (1997).
[7] D. S. Bale and C. Szeles (unpublished).
[8] T. E. Schlesinger, J. E. Toney, H. Yoon, E. Y. Lee, B. A. Brunett, L. Franks, and R. B. James, Mater. Sci. Eng., R. **32**, 103 (2001).
[9] M. Prokesch and C. Szeles, Phys. Rev. B **75**, 245204 (2007).
[10] M. Jung, J. Morel, P. Fougeres, M. Hage-Ali, and P. Siffert, Nucl. Instrum. Methods Phys. Res. A **428**, 45 (1999).
[11] Glenn F. Knoll, *Radiation Detection and Measurment* (Wiley, New York, 2000).
[12] R. J. LeVeque, CLAWPACK software, available on the Web at the URL http://www.amath.washington.edu/~claw
[13] W. J. Iles, National Radiological Protection Board Report No. NRPB-R204, 1987 (unpublished).
[14] C. Szeles, S. A. Soldner, S. Vydrin, J. Graves, and D. S. Bale, IEEE Trans. Nucl. Sci. **54**, 1350 (2007).
[15] J. Kevorkian and J. D. Cole, *Multiple Scale and Singular Perturbation Methods* (Springer-Verlag, New York, 1996).
[16] K. R. Zanio, W. M. Akutagawa, and R. Kikuchi, J. Appl. Phys. **39**, 2818 (1968).
[17] C. Szeles, Y. Y. Shan, K. G. Lynn, A. R. Moodenbaugh, and E. E. Eissler, Phys. Rev. B **55**, 6945 (1997).
[18] D. S. Bale and C. Szeles, 16th International Workshop on Room-Temperature Semiconductor X-ray and Gamma-ray Detectors, San Diego, CA, 29 October–4 November 2006 (unpublished).
[19] C. Szeles, S. A. Soldner, S. Vydrin, J. Graves, and D. S. Bale, 16th International Workshop on Room-Temperature Semiconductor X-ray and Gamma-ray Detectors, October 2006 (unpublished).